DOI: 10.1002/ ((please add manuscript number))
Full Paper

Influence of Blend Morphology and Energetics on Charge Separation and Recombination Dynamics in Organic Solar Cells Incorporating a Non-Fullerene Acceptor

*Hyojung Cha, Scot Wheeler, Sarah Holliday, Stoichko Dimitrov, Andrew Wadsworth, Hyun Hwi Lee, Derya Baran, Iain McCulloch, and James R. Durrant**

Dr. H. Cha, S. Wheeler, Dr. S. Holliday, Dr. S. Dimitrov, A. Wadsworth, Prof. I. McCulloch, Prof. J. R. Durrant
Department of Chemistry and Centre for Plastic Electronics, Imperial College London, London SW7 2AZ, United Kingdom.
E-mail: j.durrant@imperial.ac.uk

Dr. S. Dimitrov, Prof. J. R. Durrant
SPECIFIC IKC, College of Engineering, Swansea University, SA2 7AX, United Kingdom.

Dr. H. H. Lee
Pohang Accelerator Laboratory, Pohang, Gyeongbuk 37673, Republic of Korea.

Prof. D. Baran, Prof. I. McCulloch
Physical Sciences and Engineering Division, KAUST Solar Center (KSC), King Abdullah University of Science and Technology (KAUST), Thuwal, 23955-6900, Kingdom of Saudi Arabia.

Keywords: organic solar cells; non-fullerene acceptor; geminate recombination; field dependent generation; non-geminate recombination

Abstract

Non-fullerene acceptors (NFAs) are attracting increasing interest for organic solar cell applications due to their low synthesis costs, chemical tunability, and promising device efficiencies and stabilities. In blends with highly crystalline donor polymers, such NFAs have been shown to yield particularly high device voltage outputs, but typically more modest quantum yields for photocurrent generation as well as often lower fill factors (FF). In this study, we employ transient optical and optoelectronic analysis to elucidate the factors determining device photocurrent and FF in blends of the highly crystalline donor polymer PffBT4T-2OD with the promising NFA FBR or the more widely studied fullerene acceptor $PC_{71}BM$. These measurements are employed to determine the charge separation and recombination dynamics in these blends, and how these are related to blend morphology and energetics. PffBT4T-2OD:FBR devices are shown to yield device efficiencies of 7%, with higher output voltages (resulting primarily from higher LUMO level of FBR) but lower

photocurrents and FFs than PffBT4T-2OD:$PC_{71}BM$ devices. AFM and XRD data indicate similar nanomorphologies for optimised blends with both acceptors, with PffBT4T-2OD crystalline correlation length estimated as 12-14 nm. PffBT4T-2OD neat films are measured from intensity dependent singlet exciton-exciton annihilation data to have a rather long singlet exciton diffusion length of 10.9 nm. Photoluminescence quenching data indicate similar exciton dissociation yields (~ 85%) for both optimised blends, in reasonable agreement with the crystalline correlation length measured by XRD. Transient photovoltage and charge extraction measurements indicate both PffBT4T-2OD-based devices show relatively slow non-geminate recombination losses, consistent with their phase segregated morphology, and enabling efficient charge collection even for devices with relatively thick (~ 200 nm) photoactive layers. However geminate recombination losses, as measured by ultrafast transient absorption spectroscopy, are observed to be significantly higher for PffBT4T-2OD:FBR blends. This is assigned to the smaller LUMO-LUMO offset of the PffBT4T-2OD:FBR blends relative to PffBT4T-2OD:$PC_{71}BM$, resulting in the lower photocurrent generation efficiency obtained with FBR. Employing time delayed charge extraction measurements, these geminate recombination losses are observed to be field dependent, resulting in the lower FF observed with PffBT4T-2OD:FBR devices. These data therefore provide a detailed understanding of the impact of acceptor design, and particularly acceptor energetics, on organic solar cell performance. Our study concludes with a discussion of the implications of these results for the design of non-fullerene acceptors in organic solar cells.

1. Introduction

Organic solar cells (OSCs) are attracting extensive interest due to their potential as low cost, light weight, flexible and readily processed photovoltaic devices.[1-6] Most OSC devices are based on the bulk heterojunction (BHJ), a blend of an electron donating polymer with an electron accepting molecule.[7-14] Whilst fullerene derivatives have been most widely employed as electron accepting molecules, attention is now increasingly focused on alternative, non-fullerene acceptors[6,15-23], which have achieved device efficiencies of upto ~ 12%. Highly crystalline, electron donating polymers have been shown to be particularly effective at yielding efficient photovoltaic device performance with a range of both fullerene and non-fullerene acceptors.[7,8] However, the quantitative understanding of how the material crytallinity and energetics impact upon device performance remains a key challenge for the rational design of such donor and acceptor materials and the selection of optimum blend nanomorphologies. In this study, we report an analysis of these issues for blends of a highly

crystalline donor polymer, poly[(5,6-difluoro-2,1,3-benzothiadiazol-4,7-diyl)-alt-(3,3'''-di(2-octyldodecyl)-2,2';5',2'';5'',2'''-quaterthiophen-5,5'''-diyl)] (PffBT4T-2OD) with either the most widely studied fullerene acceptor, $PC_{71}BM$ or a promising non-fullerene electron acceptor, FBR (see **Figure 1** for molecular structures). We focus in particular upon the kinetics of charge separation, recombination and transport in these blends which underpin device efficiency, and how these processes are influenced by the film nanomorphology and material energetics.

We have recently reported that blends of the donor polymer PffBT4T-2DT with FBR can yield device open-circuit voltages (V_{OC}) of 1.12 V, corresponding to a remarkably low voltage loss of only 0.5 V between the optical bandgap and qV_{OC}.[24] These devices yielded power conversion efficiencies (PCE) of 7.8%, limited primarily by relatively modest external quantum efficiencies (EQE ~ 57%) and fill factors (FF ~ 61%).[24] In the study herein, we focus upon the factors limiting the EQE and FF in such crystalline donor polymer:non-fullerene acceptor devices, employing the analagous, more crystalline, donor polymer, PffBT4T-2OD. PffBT4T-2OD is a promising, widely studied donor polymer for BHJ solar cells, and exhibits, in blends with a range of acceptor molcules, promising device efficiencies ~ 11%, correlated with a high degree of crystallinity and a well-defined phase separation, with pure domains of 30−40 nm diameter.[7,8] This relatively large domain size is particularly surprising, as it exceeds the exciton diffusion length reported for most donor polymers.[7] However, studies of underlying exciton and charge carrier dynamics in blends employing this donor polymer, and how these are influenced by blend nanomorphology and choice of electron acceptor, have been absent from the literature to date.

We focus herein on blends of PffBT4T-2OD with $PC_{71}BM$ and a rhodanine-flanked non-fullerene acceptor, FBR (full name in Supporting Information).[24-26] The molecular structures and energy levels of these photoactive materials are shown in Figure 1. FBR has a relatively high lowest unoccupied molecular orbital (LUMO) compared to $PC_{71}BM$, which has been shown to result in enhanced voltage output with both P3HT[25] and PffBT4T-2DT.[24] We have reported relatively fast charge recombination losses in P3HT:FBR blends compared to P3HT:$PC_{61}BM$ blends, and suggested that these most likely originate from the relatively intermixed morphology present in the P3HT:FBR blend, as well as the smaller energy offset driving charge separation caused by the higher LUMO level of FBR.[25] In the study we report herein, we focus on the more crystalline PffBT4T-2OD:FBR blend, and in particular the extent to which exciton decay to ground, the geminate recombination of bound charges at the donor/acceptor interface and the non-geminate recombination of dissociated charges can

impact upon the short circuit photocurrent (J_{SC}) and FF of the complete devices using this blend. As such, this study provides insights into the impact of the crystallinity and energetics of photoactive materials on the performance of crystalline donor polymer:non-fullerene acceptor blend solar cells.

2. Results and Discussion

2.1. Device Current/Voltage Characterization

BHJ organic solar cells were fabricated with the inverted device structure of glass/ITO/ZnO/active layer/MoO_3/Ag, where the active layer comprised blends of PffBT4T-2OD with $PC_{71}BM$ or FBR. Current density-voltage (*J*-*V*) characteristics of optimised devices measured under AM 1.5G solar illumination at 1 sun (100 mW cm^{-2}) are shown in **Figure 2**a and summarized in **Table 1**. Figures S1-S3 show *J*-*V* data for devices prepared as a function of various processing conditions including: the ratio of donor and acceptor components, the spin-speed to adjust film thickness, and the temperatures of thermal treatments. For PffBT4T-2OD:$PC_{71}BM$ devices, these data are broadly consistent with previous reports.[7,8] Devices employing FBR showed optimal device efficiencies for rather thinner photoactive layers (~ 100 nm) compared to PffBT4T-2OD:$PC_{71}BM$ blend layers (~ 200 nm), with FBR device efficiencies being found to be relatively less sensitve to active layer thickness (Figure S2). For both blends, spincoating from 1:1.4 (wt/wt) donor:acceptor solutions in a cholobenzene:*o*-dichlorobenxene (CB:*o*-DCB, 1:1) was found to yield optimum performance. Blends with $PC_{71}BM$ required addition of 3 vol% 1,8-diiodooctane (DIO) to the processing solution for efficient devices (thought to be a processing additive to promote nanoscale phase separation); in contrast this addition degraded the performance of FBR devices. PffBT4T-2OD:FBR-blend devices exhibited a higher V_{OC} (1.11 ± 0.01 V) compared to the PffBT4T-2OD:$PC_{71}BM$-based solar cells (0.81 ± 0.01 V), assigned primarily to higher LUMO level of FBR, as well as suppressed non-radiative recombination losses.[24] It is apparent that the performance of PffBT4T-2OD:FBR devices is limited by their relatively low FF and J_{SC}, resulting in a device efficiency of ~ 7.0% compared to 10.3% for devices employing $PC_{71}BM$. Figure 2b shows the EQE spectra of corresponding devices. Integration of these spectra yielded calculated one sun photocurrents in good agreement (within 5%) of the measured J_{SC}s (11.9 mA cm^{-2} for FBR device and 18.8 mA cm^{-2} for $PC_{71}BM$ device). It is apparent that the lower J_{SC} for the PffBT4T-2OD:FBR devices result primarily from lower EQE values – with these peaking at 47% compared to 71% for PffBT4T-2OD:$PC_{71}BM$ devices.

To assign EQE spectra of both blend solar cells, the optical properties of PffBT4T-2OD-based blend films were investigated using UV–Visible absorption. The normalized UV-Visible absorption spectra of solid thin films are shown in **Figure 3a** and **3b**. PffBT4T-2OD exhibits strong absorption in the 600–750 nm region with a maximum absorption of 698 nm. In contrast, both acceptors exhibit complementary absorption in the 400-600 nm range, with FBR absorption being significantly more intense. These broad blend absorption spectra are consistent with the EQE shown in Figure 2b. It can be seen that the EQE covers a broad response of 450–750 nm for both solar cells. The EQE in the 600–750 nm range is attributed to PffBT4T-2OD absorption, whilst that in the 450–600 nm range is attributed to FBR and $PC_{71}BM$ absorption, indicating that both acceptors contribute to the photocurrent generation in these BHJ solar cells.

Plots of J_{SC} versus light intensity yielded near linear behaviour for both acceptors, with only small sub-linear deviations from linearity at high intensities (Figure S4). These data indicate that non-linear losses such as non-geminate recombination are relatively modest at short circuit for both blends, and therefore that differences in non-geminate recombinaton losses can not explain the higher J_{SC} and EQE values obtained for the PffBT4T-2OD:$PC_{71}BM$ devices. As such, we focus herein primarily on monomolecular decay processes and how these limit J_{SC} and FF. Specifically, we focus on losses associated with exciton decay to ground prior to separation at the donor:acceptor interface and on the geminate recombinaton of photogenerated charges bound at this interface.

2.2. Blend Film Morphology

PffBT4T-2OD has previously been shown to maintain its high crystallinity in blend films with a range of acceptor molecules.[7] In order to investigate any morphological differences between the PffBT4T-2OD:$PC_{71}BM$ and PffBT4T-2OD:FBR blends studied herein, grazing incidence wide angle x-ray scattering (GIWAXS) and atomic force microscopy (AFM) were used, employing the optimum device processing conditions identified above, and complimented by exciton diffusion length and photoluminescence quenching data presented in the following section. Data were collected with and without DIO. As indicated in Figure S5, all the blend films show GIWAXS peaks indicative of similar PffBT4T-2OD lamellar d-spacing (q=3.0 nm^{-1} (100)) and π–π stacking spacing (q=17.5 nm^{-1} (010)) independent of acceptor or the use of DIO. To gain quantitative insight into the structural changes, the integrated intensity of lamellar stacking (100) peak was fitted to a Gaussian profile to calculate the crystalline correlation length (CCL), a parameter related to the domain size. We

observe slightly higher CCL of Pff4TBT-2OD domain in Pff4TBT-2OD:FBR (CCL ~ 14.7 nm) as compared to Pff4TBT-2OD:$PC_{71}BM$ analogue (CCL ~ 12.9 nm) indicating a slightly larger domain size for Pff4TBT-2DT:FBR[24]. We note these domain sizes estimated herein appear a little shorter than previous soft X-ray scattering morphological studies of PffBT4T-2OD blend films by Yan and coworkers, which have indicated the formation of relatively large (upto 30-40 nm) PffBT4T-2OD domains.[7,8] The origin of this difference is unclear, it may be related to variations between PffBT4T-2OD batches and processing details.

AFM data, employed to investigate the surface morphology of these photoactive layers, are plotted as height (left) and phase (right) images in Figure S6. AFM data for optimised devices of either acceptor showed similar surface morphologies and film roughness: R_{rms}=2.9 nm for PffBT4T-2OD:$PC_{71}BM$ with DIO and R_{rms}=2.5 nm for PffBT4T-2OD:FBR without DIO. On the other hand, non-optimised films showed rougher film surface indicative of excessive phase segregation: condition, R_{rms}=7.2 nm for PffBT4T-2OD:$PC_{71}BM$ without DIO and R_{rms}=5.1 nm for PffBT4T-2OD:FBR with DIO. Whilst both optimised blend films showing similar roughness, a more fibril structure is apparent in the phase images for the PffBT4T-2OD:$PC_{71}BM$ blend film with DIO (Figure S6b), which may aid charge collection in this blend. Overall these data indicate that optimised blends with $PC_{71}BM$ and FBR acceptor exhibit similar broadly similar, as is further supported by the PL quenching data presented below.

2.3. Exciton Lifetime and Exciton Diffusion Length for PffBT4T-2OD and FBR

The PffBT4T-2OD domain sizes estimated by XRD above (13-15 nm) are larger than those typically observed in efficient organic BHJ solar cells, and also rather long relative to the exciton diffusion lengths (L_{exc}) typically reported for conjugated polymers.[27-30] As such, these large domain sizes might be expected to limit efficient exciton separation in these blend films. In order to address this issue, we employed intensity dependent ultrafast TAS measurements to measure the exciton diffusion length in neat PffBT4T-2OD and FBR films (the exciton diffusion length for $PC_{71}BM$ has previously been measured to be 3-5 nm[31,32]). This method is based on the observation of the monomolecular exciton decay to ground at low excitation densities, and bimolecular exciton-exciton annihilation at high excitation densities. These data are used to determine the exciton diffusion coefficient (D_{exc}), monomolecular exciton lifetime (τ_{exc}) and thereby $L_{exc} = (D_{exc}\,\tau_{exc})^{1/2}$ (see Supporting information and Figure S7a).[29,30] Photoexcitation of neat PffBT4T-2OD at 715 nm results in the appearance of a broad photoinduced singlet exciton absorption spectrum with a maximum at 1300 nm, **Figure**

4a. The decay of this photoinduced absorption was observed to be strongly intensity dependent, exhibiting decay half-times ranging from ~ 450 ps at the lowest usable excitation density 0.2 μJcm^{-2} to 21.5 ps at 50 μJcm^{-2} (Figure S7 and Table S1, representative data at 10 μJcm^{-2} is shown in Figure 5a). As expected, the decay dynamics are approximately mono-exponential at low excitation densities, while power laws are observed at high excitation densities. From these data, we obtain values of D_{exc} = 2.1×10^{-3} cm^2 s^{-1} and L_{exc} = 10.9 nm for PffBT4T-2OD. Analogous data for neat FBR yielded values of D_{exc} = 5.8×10^{-3} cm^2 s^{-1} and L_{exc} = 5.5 nm. The value of L_{exc} for PffBT4T-2OD is relatively large compared to those reported for other donor polymers[27-30], which typically have values closer to 5 nm, and longer than that observed herein for FBR. This long exciton diffusion length appears to result primarily from the long exciton lifetime of PffBT4T-2OD rather than faster exciton diffusion kinetics. This long lifetime is most probably associated with the relatively rigidity of PffBT4T-2OD suppressing non-radiative decay to ground. The long exciton diffusion length for PffBT4T-2OD is likely to be a key reason behind blends employing this polymer being able to achieve reasonably efficient exciton separation with relatively large, crystalline polymer domains.

Photoluminescence quenching measurements were employed to measure directly the yield of exciton dissociation in the blend. PL quenching is complimentary probe of film morphologies, with sub-unity quenching efficiencies typically resulting from exciton decay to ground during exciton diffusion to the polymer/acceptor interface. PL spectra of the pristine materials and donor:acceptor blend films prepared at optimal 1:1.4 (wt/wt) ratio are presented in Figure 3c and 3d. Following selective excitation of PffBT4T-2OD at 600 nm, both blend films exhibit reasonably strong polymer PL quenching relative to the neat polymer film, by 87% in the blend with $PC_{71}BM$ and 83% in the blend with FBR. This PL quenching is less than that typically observed in blends with more amorphous donor polymers, but similar to that observed for P3HT:$PC_{61}BM$,[25] consistent with the strongly phase segregated morphology indicated from the structural analyses detailed above. As we discuss below, this sub-unity PL quenching is assigned to exciton decay to ground during exciton diffusion, most likely resulting from the relatively large PffBT4T-2OD domain sizes. In contrast, selective excitation of FBR at 480 nm resulted in almost complete (> 99%) quenching of FBR photoluminescence, indicating relatively small FBR domains and/or that FBR domains include a significant fraction of intermixed donor polymer ($PC_{71}BM$ emission quenching could not be measured due to its low PL yield). Excitation of the FBR did not result in measurable PffBT4T-2OD emission, indicating negligible energy transfer from FBR excitons to PffBT4T-2OD. From these PLQ data and the measured exciton diffusion length of

PffBT4T-2OD, we can estimate PffBT4T-2OD domains sizes of 8 and 9 nm in blends with $PC_{71}BM$ and FBR respectively, in reasonable agreement with the domain sizes estimated from XRD data.[37] The rather smaller polymer domain sizes measured from the PLQ data compared to the XRD data most probably results from the presence of some PffBT4T-2OD in intermixed polymer:acceptor domains, which would result in the measured PLQs being overestimates of the PLQ from the pure PffBT4T-2OD domains alone.

2.4. Geminate Recombination Losses of PffBT4T-2OD-based Blends

Our PL quenching data above indicates that exciton decay to ground results in ~ 13 and 17% quenching yield losses for PffBT4T-2OD excitation of blends with $PC_{71}BM$ and FBR respectively (assuming similar PL quenching in complete devices). Whilst not insignficant efficiency losses, these losses are unable to explain the significantly higher EQEs observed for PffBT4T-2OD:$PC_{71}BM$ devices compared to PffBT4T-2OD:FBR devices (71 and and 47%, respectively). Therefore, ultrafast TAS measurements were employed to further investigate the charge separation process in PffBT4T-2OD:$PC_{71}BM$ and PffBT4T-2OD:FBR blend films. Transient absorption spectra of these blend films are presented in Figures 4b and 4c, with these data being normalised to matched densities of absorbed photons. For both blend films, the transient absorption spectra at early times exhibit a similar broad absorption to that of the neat polymer film, and are therefore assigned to PffBT4T-2OD singlet excitons. These blend spectra rapidly evolve at longer time delays to a narrower, blue shifted, photo-induced absorption with a maximum at 1100 nm, typical of polaron formation in such blend films.[31] As expected, the early time (1 ps) spectrum assigned to PffBT4T-2OD excitons is similar in ampliude for both blends. However, the amplitude of the 1100 nm polaron signal observed at long times (1 and 6 ns in Figures 4b and 4c) is significantly larger (almost two fold) for PffBT4T-2OD:$PC_{71}BM$ compared to PffBT4T-2OD:FBR. This larger amplitude can not be assigned to $PC_{71}BM$ anion absorption, which exhibits only a very weak, and red-shifted absorption.[31] These spectra therefore indicate that the PffBT4T-2OD:$PC_{71}BM$ blend exhibits a significantly higher yield of long lived polarons than the PffBT4T-2OD:FBR blend.

Figure 5 shows the corresponding transient absorption dynamics for neat polymer and both blend films at two probe wavelengths. Figure 5a compares the PffBT4T-2OD singlet exciton decay dynamics at 1300 nm in the two blend films compared to the neat polymer film. It is apparent that in both blends, the PffBT4T-2OD exciton decay kinetics are significantly faster than for the neat polymer, exhibiting decay half times of 36 and 59 ps for the blends with $PC_{71}BM$ and FBR respectively, approximately one order of magnitude faster than the

exciton decay in the neat polymer film. These data are in reasonable agreement with the PL quenching data discussed above, and with the modestedly higher exciton separation efficiency for blends with $PC_{71}BM$ compared to FBR. This difference in exciton separation is however not enough to explain the substantially higher yield of long lived charges, and higher EQE values, observed for the $PC_{71}BM$ blend compared to the FBR blend.

We turn now to the polaron decay kinetics monitored at 900 nm (Figure 5b). At early times (< 100 ps), these data are dominated by the decay of polymer exciton absorption. However these excitons have decayed by ~ 100 ps (Figure 5a) and so the remaining, long lived signal can be assigned to polaron absorption. It is apparent that for the PffBT4T-2OD:FBR blend film, this polaron signal is both smaller and decays faster than for PffBT4T-2OD:$PC_{71}BM$, indicating that both the yield and lifetime of photogenerated polarons are lower for blends with FBR compared to $PC_{71}BM$. Analagous ultrafast TAS data were also collected for selective acceptor excitation at 480 nm, as plotted in Figures 5c and S8. Again, for matched densities of photons absorbed, the yield and lifetimes of photogenerated polarons were lower for PffBT4T-2OD:FBR blends compared to PffBT4T-2OD:$PC_{71}BM$ blends, as apparent from the long time (> 100 ps) data in Figure 5c.

The polaron decay dynamics monitored in Figures 5b and 5c were measured as a function of light intensity, as plotted in Figures S9-S10 for time delays > 500 ps for excitaton densities ranging from 3.6 to 26 μJcm^{-2}. From these data it is apparent that for PffBT4T-2OD:$PC_{71}BM$, the polaron decay kinetics are significantly retarded at the lowest excitation densities, indicative of these decay dynamics resulting, at least in part from non-geminate recombination losses associated with the relatively intense pulse laser excitation. In contrast, the polaron decay dynamics for the PffBT4T-2OD:FBR blend were found to be intensity-independent, indicating they should be assigned to geminate recombination of bound polaron pairs rather than non-geminate recombination of dissociated polarons (Figure S9-S10). It can thus be concluded that the PffBT4T-2OD:FBR blend exhibits significantly greater geminate recombination losses than PffBT4T-2OD:$PC_{71}BM$ blends, and that this recombination primarily occurs on the ~ 1 ns timescale. It is also apparent that the magnitude of these geminate recombination losses are sufficient to explain the lower EQE values obtained for the PffBT4T-2OD:FBR based solar cells, although a quantitative analysis of this point requires consideration of the field dependence of these losses, as we discuss further below.

2.5. Non-Geminate Recombination Losses

The previous sections have discussed the role of exciton decay to ground and geminate recombination in determining the efficiency of PffBT4T-2OD:FBR and PffBT4T-2OD:$PC_{71}BM$ devices. We now turn to analysis of non-geminate recombination losses, how these impact upon V_{OC}, and how their competition with charge transport impacts upon device *FF*. This analysis was undertaken using transient photovoltage (TPV) and charge extraction (CE) measurements, following procedures reported previously.[34-36] The charge carrier density (n) of active layer at open circuit obtained from CE measurements as function of V_{OC}, controlled by varying the applied light intensity, is illustrated in **Figure 6**a. $n(V_{OC})$ describes the density of charge carriers accumulated for a particular quasi-Fermi level splitting within the active layer, and is therefore an *in situ* assay of the blends effective electronic bandgap. For both devices, n was observed to increase exponentially with V_{OC}, consistent with this charge primarily accumulating in shallow trap/tail states, as is typical of organic BHJ's. At a representative n of 1.4×10^{16} (corresponding to approx. one sun irradiation), a shift of +0.24 V is observed between the PffBT4T-2OD:$PC_{71}BM$ and PffBT4T-2OD:FBR devices. This increase in effective electronic bandgap is consistent with higher LUMO levels of FBR relative to $PC_{71}BM$; we note this *in situ* measurement of a 0.24 V shift is smaller than the LUMO shift estimated from neat film CV data (Figure 1), most likely due to differing material energetics between neat and blend films.[37,38] Figure 6b shows charge carrier lifetimes τ as measured by TPV, as a function of carrier density. Comparing at the same equivalent carrier density of $n = 1.4 \times 10^{16}$, the non-geminate recombination lifetime is approximately seven times longer for the PffBT4T-2OD:FBR device compared to PffBT4T-2OD:$PC_{71}BM$ device. This slower carrier recombination results in a further 0.054 V calculated[39,40] increase in the FBR device V_{OC} in addition the energetic shift, as it enables higher charge accumulation and therefore a larger quasi-Fermi level splitting. Overall these analyses of the impact of materials energetics and non-geminate recombination on device V_{OC} are in reasonable agreement with the 0.3 V increase in V_{OC} measured directly under one sun irradiation (Table 1).

We now turn to consideration of charge transport in these devices. The effective drift mobility (μ) of PffBT4T-2OD-based solar cells was calculated from measurements of charge carrier density at short-circuit (n_{SC}) measured using CE as described previously.[39,40] Figure 6c shows the effective drift mobility of PffBT4T-2OD:acceptor systems plotted over the range of n_{SC}. PffBT4T-2OD:FBR devices show three times lower drift mobility at the equivalent carrier density compared to PffBT4T-2OD:$PC_{71}BM$ devices, most probably associated with trap behavior despite the similar electron mobility.[25] Combining these

mobility data with the carrier lifetime data shown in Figure 6b, we obtain values for the $\mu\tau$ product of PffBT4T-2OD:FBR device which are 2-3 times larger than those for PffBT4T-2OD:$PC_{71}BM$ device. An alternative viewpoint is to quantify the extent to which the measured non-geminate recombination deviates from simple Langevin recombination theory.[41-43] Figure 6d shows the measured bimolecular recombination coefficient (k_{bi}) compared to that predicted from Langevin theory (k_L), plotted as function of charge density. Both blends show k_{bi} values substantially less than k_L thus displaying non-Langevin behaviour indicating suppressed bimolecular recombination. The PffBT4T-2OD:FBR device (k_{bi}/k_L = 0.05) shows slightly more non-Langevin behaviour compared to the PffBT4T-2OD:$PC_{71}BM$ device (k_{bi}/k_L = 0.1), as shown in Figure S10a, consistent with the $\mu\tau$ product analysis. These data suggest that the impact of kinetic competition between charge transport and non-geminate recombination in limiting charge collection, and therefore device FF should be less severe for FBR devices compared to $PC_{71}BM$ devices. This contrasts to the measured FFs of 0.5 and 0.65 for the FBR and $PC_{71}BM$ devices respectively, and strongly indicates that the lower FF of the FBR device does not result from less efficient charge collection. We discuss alternative limitations to this FF below.

2.6. Field Dependence of Photogeneration

Despite increased non-Langevin behaviour in the PffBT4T-2OD:FBR blend, which should result in more efficient charge extraction, the FF (~ 50%) of the PffBT4T-2OD:FBR device is lower than that of the PffBT4T-2OD:$PC_{71}BM$ device (~ 65%). As discussed above, our ultrafast transient absorption data on blend films indicate that the FBR blend exhibits more severe geminate recombination losses than the $PC_{71}BM$ blend. We now consider whether these geminate recombination losses in PffBT4T-2OD:FBR devices are field dependent and therefore explain the lower FF's observed for these devices. Considering the corrected photocurrent in **Figure 7**a ($J_{CP}(V)=J_{light}(V)-J_{dark}(V)$, measured under pulsed conditions to negate effects of device heating) for both devices, it is apparent that whilst the corrected photocurrent of the FBR device at short circuit is lower, it increases strongly under strong reverse bias, and by -16 V exceeds that of $PC_{71}BM$ devices. This behaviour would be consistent with field dependent charge generation for the PffBT4T-2OD:FBR devices in the absence of strong non-geminate recombination in this regime. In order to probe directly the potential presence of field dependent charge generation in the PffBT4T-2OD:FBR devices, we employed the time delayed collection field (TDCF) measurement.[44-46] Following charge generation from a nanosecond laser pulse at a controlled pre-bias (V_{pre}), generated charge is

extracted after a time delay (t_d) by switching to a reverse collection bias (V_{rev}). At short delay times of ~ 10 ns and under low excitation densities, it is possible to extract the generated charges prior to significant non-geminate recombination losses. Comparing the extracted charges at different pre-bias conditions allows observation of any field dependence in generation. Figure S11 shows the total charge (Q_{tot}) remaining in the system as a function of switching time t_d. At early t_ds, a plateau is present, indicating these time delays are prior to the onset of non-geminate recombination. Comparing Q_{tot} values for different pre-bias conditions, a field dependent profile normalised at short-circuit is shown in figure 7b. These data indicate a clear field dependence of charge generation for the PffBT4T-2OD:FBR device, corresponding to a 15% reduction in charge generation between short circuit and open circuit. This can be assigned to field dependent geminate recombination losses, with these enhanced losses most likely resulting from the smaller LUMO-LUMO offset present in the PffBT4T-2OD:FBR devices as discussed above. As illustrated in Figure S12, this field dependence is sufficient to be the primary cause of the lower FF of the PffBT4T-2OD:FBR devices compared to the PffBT4T-2OD:$PC_{71}BM$ devices.

3. Summary and Conclusions

Herein we report the effect of phase separation morphology and energetics on charge separation and recombination dynamics in PffBT4T-2OD-based BHJ solar cells, and the impact of these kinetics upon device photovoltaic performance. PffBT4T-2OD:FBR blend devices exhibited a higher V_{OC} due to high-lying LUMO level of FBR as well as suppressed non-radiative recombination losses relative to the PffBT4T-2OD:$PC_{71}BM$-based solar cells. However, the device performance of PffBT4T-2OD:FBR blend is still limited by their relatively low FF and J_{SC}, resulting in a device efficiency of ~ 7.0% compared to 10.3% for devices employing $PC_{71}BM$. In this article, we addressed key issues determining device photocurrent and FF for PffBT4T-2OD:FBR device. Previous literature has shown that higher geminate recombination losses can typically be caused by excessively intermixed nanomorphologies.[33] GIWAXS and PL quenching data indicate highly crystalline polymer phase in the nanomorphologies for optimised PffBT4T-2OD blends with either $PC_{71}BM$ or FBR. Moreover, we find that the PffBT4T-2OD is able to acheive effective exciton diffusion and separation even in the presence of relatively large pure polymer domains due to its relatively long exciton lifetime and diffusion length (10.9 nm). As discussed above, the similar PL quenching efficiency observed for the PffBT4T-2OD:FBR and PffBT4T-2OD:$PC_{71}BM$ blends studied herein suggests that nanomorphology is not the cause of the

higher geminate losses for PffBT4T-2OD:FBR, at least following polymer photoexcitation. Rather it appears very likely that these higher geminate losses result from the higher LUMO level of FBR relative to $PC_{71}BM$, reducing the excess energy available to drive electrons away from the donor/acceptor interface. We note that in either case, these data, combined with our PL quenching data above, provide clear evidence that the primary factor reducing the efficiency of generating dissociated charges for PffBT4T-2OD:FBR blends is not the efficiency or kinetics of exciton separation at the donor/acceptor interface. Rather it is the ability of the charges generated by this exciton separation to escape this interface, and thereby avoid the formation, and subsequent recombination, of geminate, bound polaron pairs formed at this interface. Whilst both PffBT4T-2OD blends exhibit similar blend morphologies and exciton dissociation yields, the PffBT4T-2OD:FBR blend is shown to exhibit a lower yield of long lived polarons due to higher, and field dependent, geminate recombination losses, leading to a relatively lower device J_{SC} and FF. These higher geminate recombination losses are attributed to higher LUMO energy level of FBR relative to $PC_{71}BM$, resulting in too small a LUMO-LUMO energy offset for efficient charge dissociation in PffBT4T-2OD:FBR blends and devices. The highly crystalline donor polymer PffBT4T-2OD results in a highly phase segregated blend nanomorphology, with relatively large polymer domains. The data herein indicates that this morphology results in relatively slow non-geminate recombination losses, enabling efficient charge collection even for thick photoactive layers. This morphology does result in some exciton losses (~ 15%) during polymer exciton diffusion to acceptor interfaces, although the magnitude of these losses are reduced by the relatively long exciton diffusion length for PffBT4T-2OD. The use of NFAs facilitates the tuning of acceptor LUMO level. This strategy has been employed to enhance device V_{OC} and has proved particularly effective with the relatively wide bandgap donor P3HT. However, with lower bandgap donors such as PffBT4T-2OD, which exhibit lower LUMO levels, this can result in very small LUMO-LUMO offsets. The data herein indicates that whilst PffBT4T-2OD:FBR exhibits reasonably efficient, exciton diffusion limited, charge generation from PffBT4T-2OD excitons, the blend exhibits significant geminate recombination losses which limit device photocurrent and fill factor. These higher geminate recombination losses can be assigned most obviously to the smaller LUMO-LUMO offset. As such, these data suggest that a key consideration for blends of NFAs with lower bandgap donor polymers is to optimise NFA LUMO level such as to achieve the maximal device V_{OC} whilst still maintaining a higher enough LUMO-LUMO offset to drive efficient charge dissociation, consistent with our recent report of higher device efficiencies in blends of PffBT4T-2DT with the intermediate LUMO level NFA IDTBR.[15,16]

4. Experimental Section

Device preparation and characterization: Prepatterned ITO-coated glass with a sheet resistance of ≈15 Ω square^{-1} (PsioTec Ltd, UK) was used as the substrate. It was cleaned by sequential sonications in detergent, DI water, acetone, and isopropanol for 5 min at each step. After oxygen plasma for 8 min at 100 W, a ZnO electron transport layer (40 nm) was prepared by spin-coating at 4000 rpm from a ZnO precursor solution (diethyl zinc). Active layer solutions (D:A ratio 1:1.4, 14 mg mL^{-1}) were prepared in CB:DCB (1:1 volume ratio) with or without 3 vol% of DIO. To completely dissolve the polymer, the active layer solution should be stirred on a hot plate at 110 °C for at least 3 h. Active layers were spin-coated from the warm polymer solution on the preheated substrate in a nitrogen glovebox at different spin rate, where MoO_3 (10 nm)/Ag (100 nm) electrodes were deposited by thermal evaporation under vacuum. Device area was 0.045 cm^2. *J–V* characteristics were measured using a Xenon lamp at AM1.5 solar illumination (Oriel Instruments) calibrated to a silicon reference cell with a Keithley 2400 source meter, correcting for spectral mismatch. A calibrated reference silicon photodiode was used as a reference for the *J–V* measurements. Incident photon conversion efficiency was measured by a 100 W tungsten halogen lamp (Bentham IL1 with Bentham 605 stabilized current power supply) coupled to a monochromator with computer controlled stepper motor. The photon flux of light incident on the samples was calibrated using a UV-enhanced silicon photodiode. A 590-nm long-pass glass filter was inserted into the beam at illumination wavelengths longer than 580 nm to remove light from second-order diffraction. Measurement duration for a given wavelength was sufficient to ensure the current had stabilized.

UV-Vis absorption and Photoluminescence (PL) spectroscopies: UV-Visible spectra of the thin films were acquired with a PerkinElmer Lambda 25 spectrometer in air. The PL spectra were measured with a Fluorolog-3 spectrofluorometer (Horiba Jobin Yvon). All film samples were spin cast on glass substrates.

AFM characterization: AFM measurements were performed by using a Scanning Probe Microscope-Dimension 3100. All film samples were spin casted on ITO/ZnO substrates.

GIWAXS Characterization: GIWAXS measurements were performed at beamline 5A at the pohang accelerator laboratory (PAL) in South Korea. Samples were prepared on ITO/ZnO

substrates using identical blend solutions as those used in devices. The 10 keV X-ray beam was incident at a grazing angle of 0.12°–0.16°, selected to maximize the scattering intensity from the samples. The scattered X-rays were detected using a Dectris Pilatus 2M photon counting detector.

Transient absorption spectroscopy: Femtosecond TAS was carried out using a commercially available transient absorption spectrometer, HELIOS (Ultrafast systems). Samples were excited with a pulse train generated by an optical parametric amplifier, TOPAS (Light conversion). Both, the spectrometer and the parametric amplifier were seeded with an 800 nm, <100 femtosecond pulses at 1 KHz generated by a Solstice Ti:Sapphire regenerative amplifier (Newport Ltd).

TPV and TDCF: Charge extraction was performed at open circuit under different illumination intensities. In addition, for J–V reconstruction, the device voltage was varied using Keithley 2400 sourcemeter, before extracting charges at short circuit. Devices were illuminated by a ring of white LEDs, where the LEDs are switched off (100 ns) and the device discharged close to short circuit over a measurement resistance of 50 O. The resulting transients were acquired with a TDS 3032 Tektronix digital oscilloscope, converted to a current using Ohm's law and integrated with respect to time to calculate n.

Transient photovoltage was recorded in an open circuit under different illumination intensities, provided by a ring of white LEDs. A Nd:YAG pulsed laser (Continuum Minilite II) was used to generate small perturbations in the device and the resulting voltage transients were recorded with a TDS 3032 Tektronix digital oscilloscope and fitted with a single exponential function to obtain a carrier lifetime. Transient photocurrent was performed in a short circuit under different illumination intensities.

Supporting Information

Device optimisation, GIWAXS data, AFM images, calculation of exciton diffusion lengths, transient absorption spectra, TDCF data are included in Supporting Information. Supporting Information is available from the Wiley Online Library or from the author.

Acknowledgements

The authors gratefully acknowledge funding from supported by KAUST under the Grant Agreement number OSR-2015-CRG4-2572 and the EU FP7 project CHEETAH, and thank Pabitra Shakya for assistance in device fabrication.

Received: ((will be filled in by the editorial staff))
Revised: ((will be filled in by the editorial staff))
Published online: ((will be filled in by the editorial staff))

[1] H. Hu, K. Jiang, G. Yang, J. Liu, Z. Li, H. Lin, Y. Liu, J. Zhao, J. Zhang, F. Huang, Y. Qu, W. Ma, H. Yan, *J. Am. Chem. Soc.*, **2015**, *137*, 14149.

[2] Z. C. He, B. Xiao, F. Liu, H. B. Wu, Y. L. Yang, S. Xiao, C. Wang, T. P. Russell, Y. Cao, *Nat. Photonics* **2015**, *9*, 174.

[3] V. Vohra, K. Kawashima, T. Kakara, T. Koganezawa, I. Osaka, K. Takimiya, H. Murata, *Nat. Photonics* **2015**, *9*, 403.

[4] J. D. Chen, C. H. Cui, Y. Q. Li, L. Zhou, Q. D. Ou, C. Li, Y. F. Li, J. X. Tang, *Adv. Mater.* **2015**, *27*, 1035.

[5] W. Zhao, D. Qian, S. Zhang, S. Li, O. Inganäs, F. Gao, J. Hou, *Adv. Mater*. **2016**, *28*, 4734.

[6] S. Li, L. Ye, W. Zhao, S. Zhang, S. Mukherjee, H. Ade, J. Hou, *Adv. Mater.* **2016**, *28*, 9423.

[7] Y. Liu, J. Zhao, Z. Li, C. Mu, W. Ma, H. Hu, K. Jiang, H. Lin, H. Ade, H. Yan, *Nat. Commun.* **2014**, *5*, 5293.

[8] W. Ma, G. F. Yang, K. Jiang, J. H. Carpenter, Y. Wu, X. Y. Meng, T. McAfee, J. B. Zhao, C. H. Zhu, C. Wang, H. Ade, H. Yan, *Adv. Energy Mater.* **2015**, *5*, 1501400.

[9] J. Zhao, Y. Li, A. Hunt, J. Zhang, H. Yao, Z. Li, J. Zhang, F. Huang, H. Ade, H. Yan, *Adv. Mater.* **2016**, *28*, 1868.

[10] J. Liu, S. Chen, D. Qian, B. Gautam, G. Yang, J. Zhao, J. Bergqvist, F. Zhang, W. Ma, H. Ade, O. Inganas, K. Gundogdu, F. Gao, H. Yan, 2016. Fast charge separation in a non-fullerene organic solar cell with a small driving force. *Nat. Energy*, **2016**, *1*, 16089-1.

[11] Y.-J. Hwang, B. A. E. Courtright, A. S. Ferreira, S. H. Tolbert, S. A. Jenekhe, *Adv. Mater.* **2015**, *27*, 4578.

[12] J. Lee, R. Singh, D. H. Sin, H. G. Kim, K. C. Song, K. Cho, *Adv. Mater.* **2016**, *28*, 69.

[13] Y. Lin, J. Wang, Z.-G. Zhang, H. Bai, Y. Li, D. Zhu, X. Zhan, *Adv.Mater.* **2015**, *27*, 1170.

[14] J. D. Douglas, M. S. Chen, J. R. Niskala, O. P. Lee, A. T. Yiu, E. P. Young, J. M. J. Fréchet, *Adv. Mater.* **2014**, *26*, 4313.

[15] S. Holliday, R. S. Ashraf, A. Wadsworth, D. Baran, S. A. Yousaf, C. B. Nielsen, C. H. Tan, S. D. Dimitrov, Z. Shang, N. Gasparini, M. Alamoudi, F. Laquai, C. J. Brabec, A. Salleo, J. R. Durrant, I. McCulloch, *Nat. Commun.*, **2016**, *7*, 11585.

[16] D. Baran, R. S. Ashraf, D. A. Hanifi, M. Abdelsamie, N. Gasparini, J. A. Röhr, S. Holliday, A. Wadsworth, S. Lockett, M. Neophytou, C. J. Emmott, J. Nelson, C. J. Brabec, A. Amassian, A. Salleo, T. Kirchartz, J. R. Durrant, I. McCulloch, *Nat. Mater.* **2016**, *16*, 363.

[17] A. Wadsworth, R. S. Ashraf, M. Abdelsamie, S. Pont, M. Little, M. Moser, Z. Hamid, M. Neophytou, W. Zhang, A. Amassian, J. R. Durrant, D. Baran, I. McCulloch, *ACS Energy Lett.*, **2017**, *2*, 1494.

[18] S. Chen, H. J. Cho, J. Lee, Y. Yang, Z.-G. Zhang, Y. Li, C. Yang, *Adv. Energy Mater.* **2017**, 1701125.

[19] B. Guo, W. Li, X. Guo, X. Meng, W. Ma, M. Zhang, Y. Li, *Adv. Mater.* **2017**, *29*, 1702291.

[20] T. Liu, X. Pan, X. Meng, Y. Liu, D. Wei, W. Ma, L. Huo, X. Sun, T. H. Lee, M. Huang, H. Choi, J. Y. Kim, W. C. H. Choy, Y. Sun, *Adv. Mater.* **2017**, *29*, 1604251.

[21] F. Zhao, S. Dai, Y. Wu, Q. Zhang, J. Wang, L. Jiang, Q. Ling, Z. Wei, W. Ma, W. You, C. Wang, X. Zhan, *Adv. Mater.* **2017**, *29*, 1700144.

[22] H. Yao, L. Ye, J. Hou, B. Jang, G. Han, Y. Cui, G. M. Su, C. Wang, B. Gao, R. Yu, H. Zhang, Y. Yi, H. Y. Woo, H. Ade, J. Hou, *Adv. Mater.* **2017**, *29*, 1700254.

[23] B. Fan, K. Zhang, X.-F. Jiang, L. Ying, F. Huang, Y. Cao, *Adv. Mater.* **2017**, *29*, 1606396.

[24] D. Baran, T. Kirchartz, S. Wheeler, S. Dimitrov, M. Abdelsamie, J. Gorman, R. S. Ashraf, S. Holliday, A. Wadsworth, N. Gasparini, P. Kaienburg, H. Yan, A. Amassian, C. J. Brabec, J. R. Durrant, I. McCulloch, *Energy Environ. Sci.*, **2016**, *9*, 3783.

[25] S. Holliday, R. S. Ashraf, C. B. Nielsen, M. Kirkus, J. A. Rö hr, C.-H. Tan, E. Collado-Fregoso, A.-C. Knall, J. R. Durrant, J. Nelson, I. McCulloch, *J. Am. Chem. Soc.* **2015**, *137*, 898.

[26] C. B. Nielsen, S. Holliday, H.-Y. Chen, S. J. Cryer, I. McCulloch, *Acc. Chem. Res.* **2015**, *48*, 2803.

[27] M. Oleksandr V., P. W. M. Blom, T.-Q. Nguyen, *Energ. Environ. Sci.*, **2015**, *8*, 1867.

[28] S. D. Dimitrov, B. C. Schroeder, C. B. Nielsen, H. Bronstein, Z. Fei, I. McCulloch, M. Heeney, J. R. Durrant, *Polymers*, **2016**, *8*, 14.

[29] A. J. Lewis, A. Ruseckas, O. P. M. Gaudin, G. R. Webster, P. L. Burn, I. D. W. Samuel, *Org. Electron. Phys., Mater. Appl.*, 2006, 7, 452.

[30] E. Collado-Fregoso, F. Deledalle, H. Utzat, P. S. Tuladhar, S. D. Dimitrov, A. Gillett, C.-H. Tan, W. Zhang, I. McCulloch, J. R. Durrant, *Adv. Funct. Mater.*, **2017**, *27*, 1604426.

[31] S. D. Dimitrov, Z. Huang, F. Deledalle, C. B. Nielsen, B. C. Schroeder, R. S. Ashraf, S. Shoaee, I. McCulloch, J. R. Durrant, *Energy Environ. Sci.* **2014**, *7*, 1037.

[32] S. Cook, A. Furube, R. Katoh, L. Han, *Chem. Phys. Lett.*, **2009**, *478*, 33.

[33] S. D. Dimitrov, J. R. Durrant, *Chem. Mater.* **2014**, *26*, 616.

[34] S. D. Dimitrov, S. Wheeler, D. Niedzialek, B. C. Schroeder, H. Utzat, J. M. Frost, J. Yao, A. Gillett, P. S. Tuladhar, I. McCulloch, J. Nelson, J. R. Durrant, *Nat. Commun.* **2015**, *6*, 6501.

[35] T. Kirchartz, F. Deledalle, P. S. Tuladhar, J. R. Durrant, J. Nelson, *J. Phys. Chem. Lett.* **2013**, *4*, 2371.

[36] D. Credgington, F. C. Jamieson, B. Walker, T.-Q. Nguyen, J. R. Durrant, *Adv. Mater.* **2012**, *24*, 2135.

[37] F. C. Jamieson, E. B. Domingo, T. McCarthy-Ward, M. Heeney, N. Stingelin, J. R. Durrant, *Chem. Sci.*, **2012**, *3*, 485.

[38] S. Sweetnam, K. R. Graham, G. O. Ngongang Ndjawa, T. Heumüller, J. A. Bartelt, T. M. Burke, W. Li, W. You, A. Amassian, M. D. McGehee, *J. Am. Chem. Soc.* **2014**, *136*, 14078.

[39] C. G. Shuttle, R. Hamilton, J. Nelson, B. C. O'Regan, J. R. Durrant, *Adv. Funct. Mater.*, **2010**, *20*, 698.

[40] C. G. Shuttle, B. O'Regan, A. M. Ballantyne, J. Nelson, D. D. C. Bradley, J. de Mello, J. R. Durrant, *Appl. Phys. Lett.*, **2008**, *92*, 093311.

[41] T. Kirchartz, T. Agostinelli, M. Campoy-Quiles, W. Gong, J. Nelson, *J. Phys. Chem. Lett.*, **2012**, *3*, 3470.

[42] G. Lakhwani, A. Rao, R. H. Friend, *Annu. Rev. Phys. Chem.*, **2014**, *65*, 557.

[43] T. M. Burke, S. Sweetnam, K. Vandewal, M. D. McGehee, *Adv. Energy Mater.*, **2015**, *5*, 1500123.

[44] J. Kniepert, M. Schubert, J. C. Blakesley, D. Neher, *J. Phys. Chem. Lett.*, **2011**, *2*, 700.

[45] J. Kniepert, I. Lange, N. J. van der Kaap, L. J. A. Koster, D. Neher, *Adv. Energy Mater.*, **2014**, *4*, 1301401.

[46] A. Foertig, J. Kniepert, M. Gluecker, T. Brenner, V. Dyakonov, D. Neher, C. Deibel, *Adv. Funct. Mater.*, **2014**, *24*, 1306.

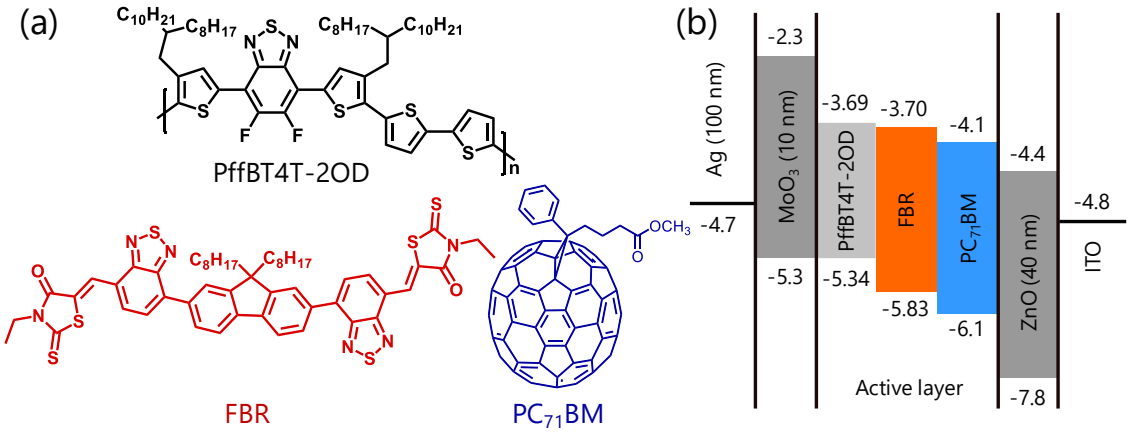

Figure 1. (a) Chemical structures of PffBT4T-2OD as an electron donor material and FBR and $PC_{71}BM$ as electron acceptors, (b) energy levels of the materials used in this work from thin films; HOMO levels measured by cyclic voltammetry and LUMO levels calculated based on HOMO levels and optical bandgap.[7,25]

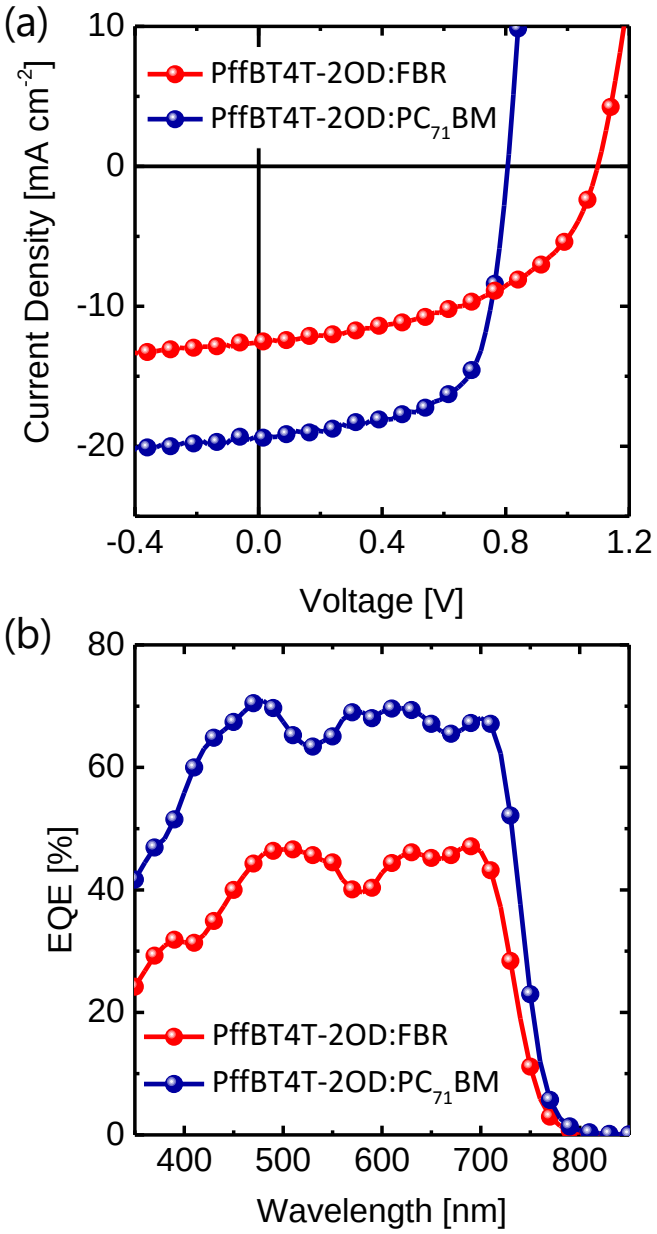

Figure 2. (a) *J-V* characteristics under illumination of AM 1.5 G, 100 mW/cm^2 and (b) EQE spectra of solar cell devices: PffBT4T-2OD:FBR without processing additives and PffBT4T-2OD:$PC_{71}BM$ with 3 vol% of DIO.

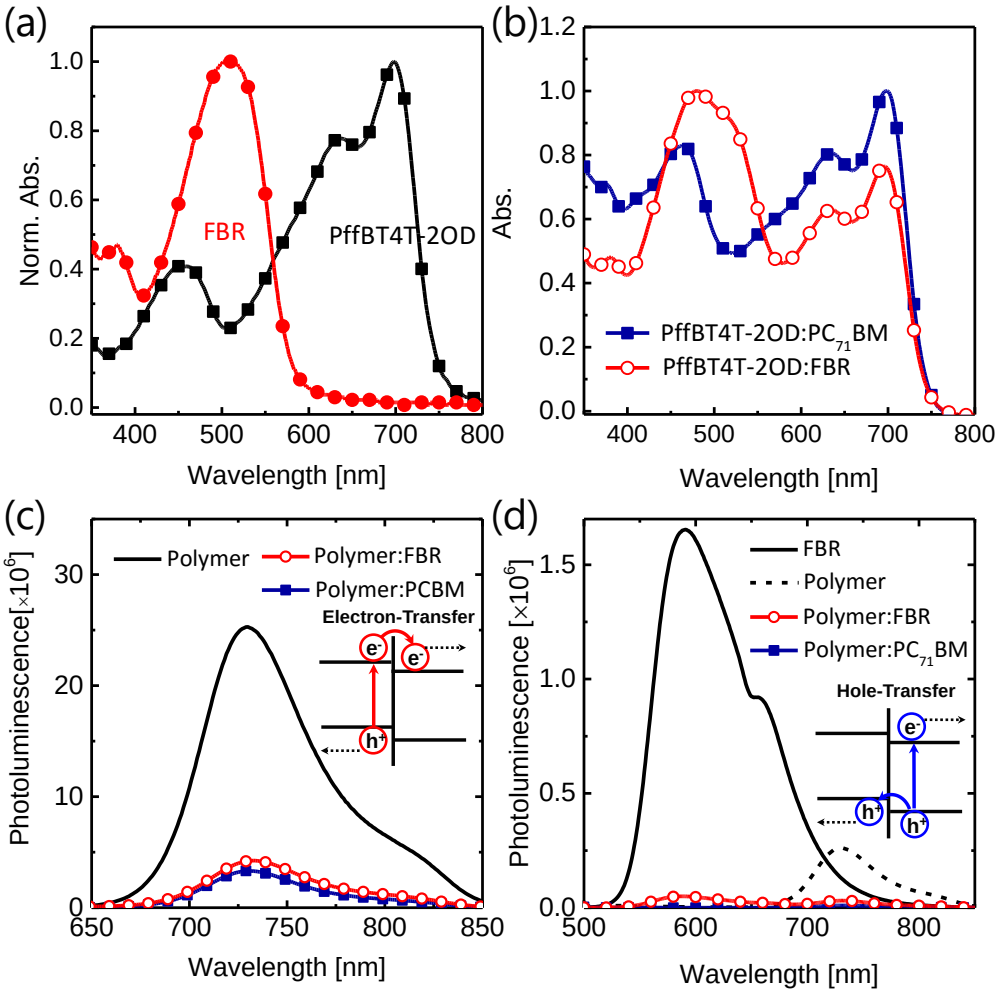

Figure 3. Normalised UV-Visible absorption spectra of (a) neat films of PffBT4T-2OD and FBR, and (b) PffBT4T-2OD:$PC_{71}BM$ blend films with 3 vol% DIO (~200 nm) and PffBT4T-2OD:FBR (~100 nm) blend films without processing additives, respectively. Steady state PL spectra of films excited on (c) polymer at 600 nm and (d) non-fullerene acceptor at 480 nm.

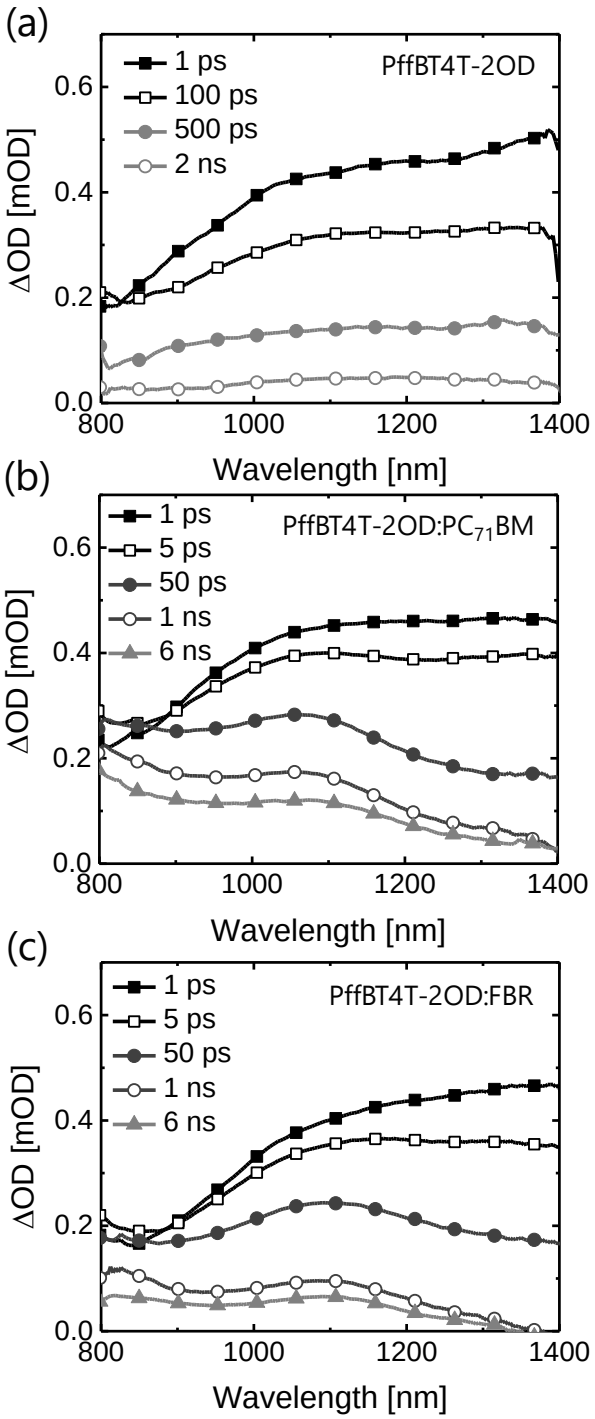

Figure 4. fs-transient absorption spectra of (a) neat polymer film, (b) PffBT4T-2OD:$PC_{71}BM$ blend film, and (c) PffBT4T-2OD:FBR blend film, excited at 715 nm with number of photons absorbed of 6×10^{17} cm^{-3}.

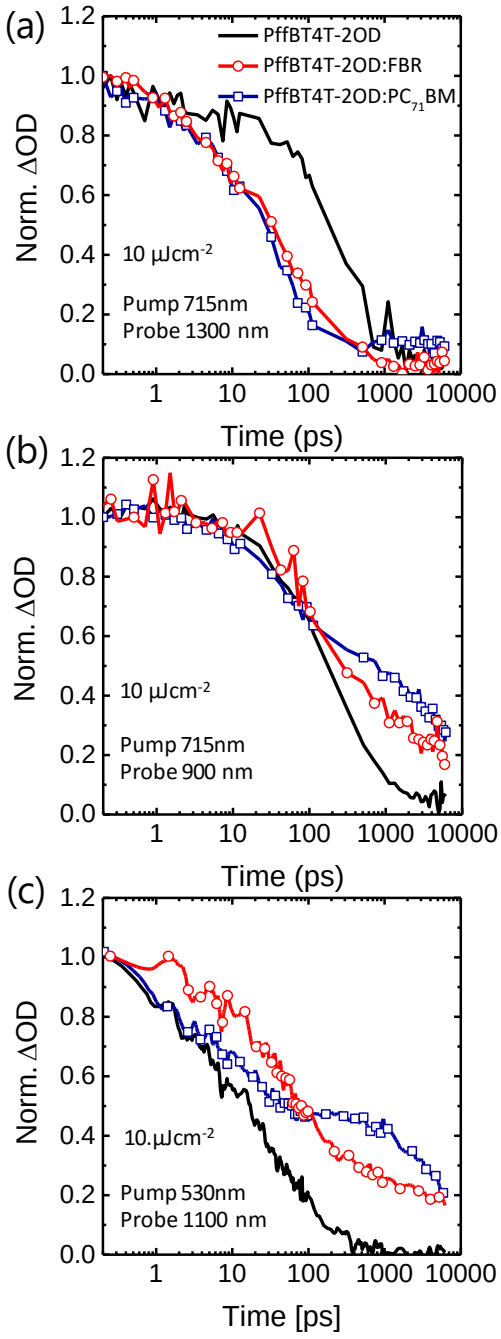

Figure 5. Transient absorption decay dynamics for neat polymer film, PffBT4T-2OD:$PC_{71}BM$ blend film, and PffBT4T-2OD:FBR blend film (a) excited at 715 nm and probed at 1300 nm and (b) excited at 715 nm and probed at 900 nm, and (c) excited at 530 nm and probed at 1100 nm.

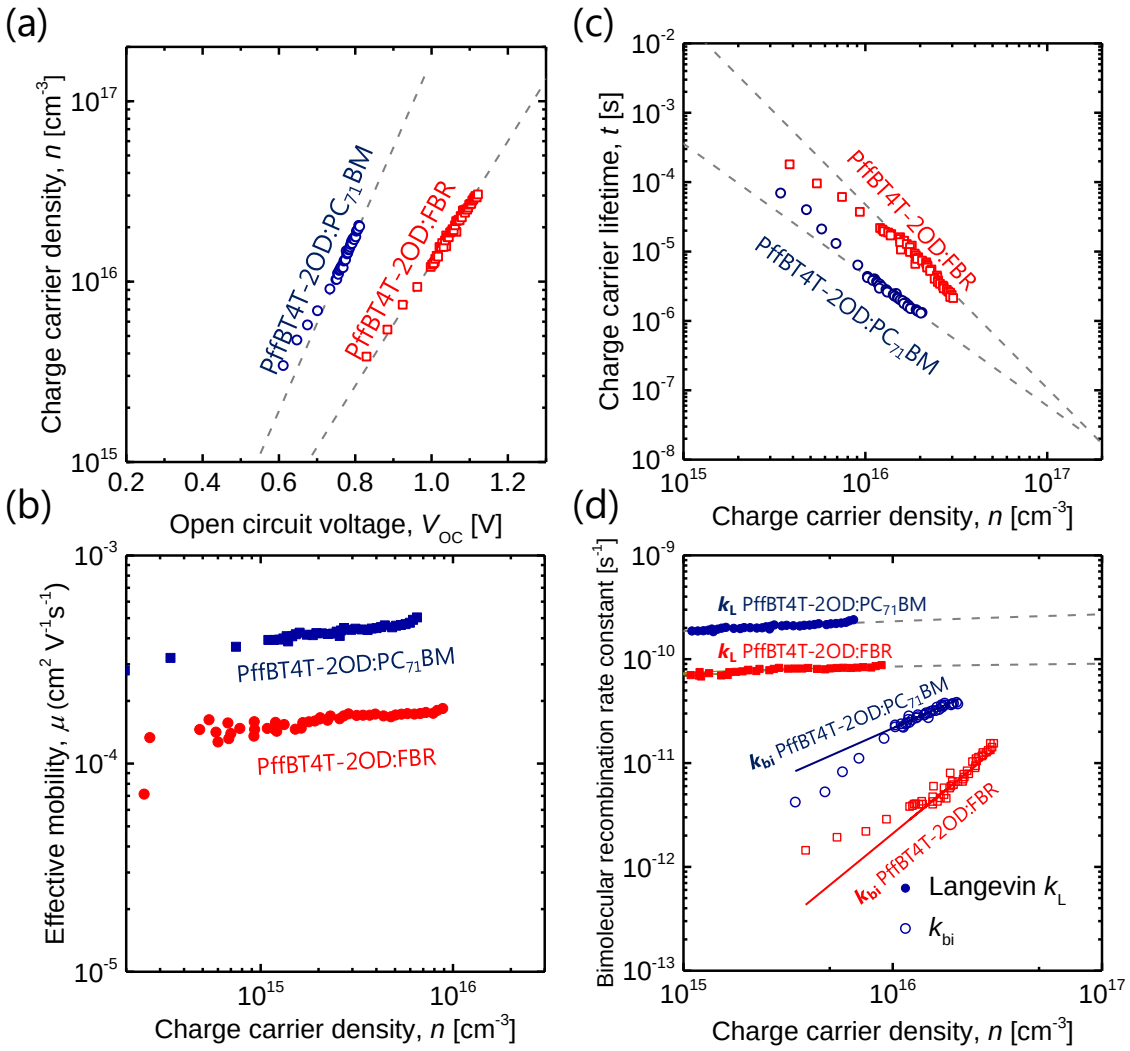

Figure 6. Analysis of recombination and transport in PffBT4T-2OD-based devices. (a) Dependence on open circuit voltage, (b) the corresponding charge carrier lifetimes measured by TPV decays, plotted against the measure charge densities, and (c) effective device mobility as a function of charge carrier density, measured by CE as short circuit for PffBT4T-2OD:$PC_{71}BM$ and PffBT4T-2OD:FBR, respectively. (d) Langerin reduction factor from measured bimolecular recombination rate which is obtained from TPV and CE at open circuit.

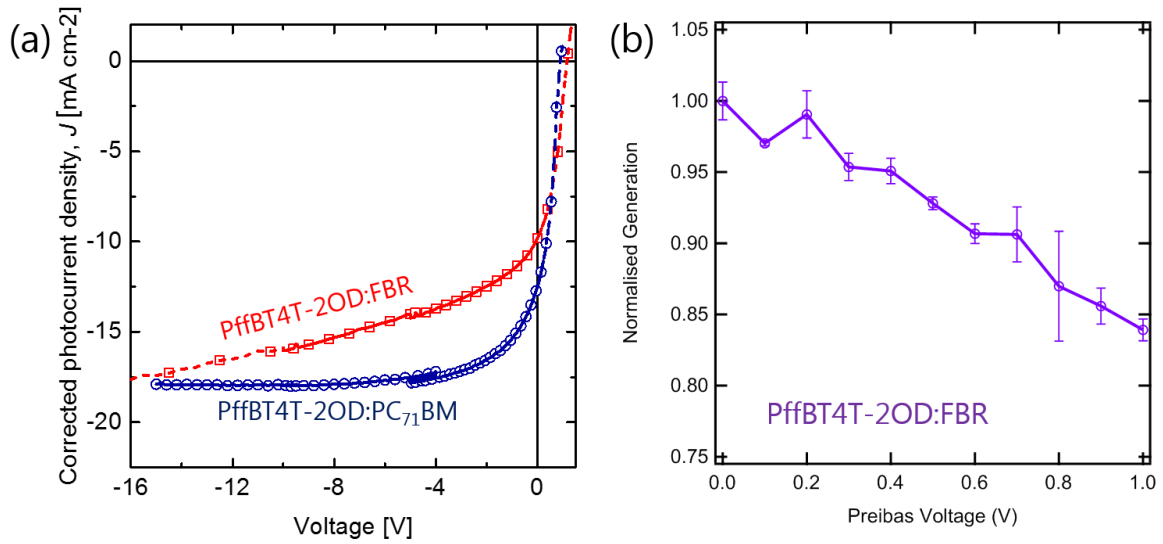

Figure 7. (a) Corrected photocurrent characteristics (-16 ~ 0V) of PffBT4T-2OD:$PC_{71}BM$, and PffBT4T-2OD:FBR devices, and (b) normalized field dependent photogeneration in PffBT4T-2OD:FBR devices.

Table 1. Device characteristics of PffBT4T-2OD:acceptor blends.

Blends[a)]	Processing Additives	J_{SC} [mA cm-2]	V_{OC} [V]	FF	PCE_{ave} [%]	PCE_{max} [%]
PffBT4T-2OD:FBR	None	12.62 (± 0.3)	1.11 (± 0.01)	0.50 (± 0.2)	6.74 (± 0.3)	7.04
	DIO 3 vol%	12.29 (± 0.3)	1.09 (± 0.01)	0.44 (± 0.3)	5.41 (± 0.5)	5.92
PffBT4T-2OD:$PC_{71}BM$	None	19.02 (± 0.5)	0.79 (± 0.01)	0.44 (± 0.5)	6.35 (± 0.3)	6.61
	DIO 3 vol%	19.38 (± 0.4)	0.81 (± 0.01)	0.65 (± 0.2)	9.80 (± 0.4)	10.23

a) The optimized weight ratio of polymer and acceptor is 1:1.4; b) The PCE values are averages from over ten devices.

The table of contents entry should be 50–60 words long, and the first phrase should be bold.

Charge separation and recombination dynamics in relation to film morphology and energetics are reported in non-fullerene-based PffBT4T-2OD:FBR solar cell. PffBT4T-2OD shows efficient exciton diffusion to the interface between the electron donors and the acceptors. Its small energetic offset explain relatively lower current density and FF correlated with geminated recombination and field dependent photogeneration.

Keyword organic solar cells; non-fullerene acceptor; geminate recombination; field dependent generation; non-geminate recombination

Hyojung Cha, Scot Wheeler, Sarah Holliday, Stoichko Dimitrov, Andrew Wadsworth, Hyun Hwi Lee, Derya Baran, Iain McCulloch, and James R. Durrant*

Influence of Blend Morphology and Energetics on Charge Separation and Recombination Dynamics in Organic Solar Cells Incorporating a Non-Fullerene Acceptor

ToC figure ((Please choose one size: 55 mm broad × 50 mm high **or** 110 mm broad × 20 mm high. Please do not use any other dimensions))